Nano Res. 2012, 5(10): 679–694
DOI 10.1007/s12274-012-0252-z
Research Article

ISSN 1998-0124
CN 11-5974/O4

Hollow Manganese Phosphate Nanoparticles as Smart Multifunctional Probes for Cancer Cell Targeted Magnetic Resonance Imaging and Drug Delivery

Jing Yu[1], Rui Hao[1], Fugeng Sheng[2] (✉), Lili Xu[2], Gongjie Li[2], and Yanglong Hou[1] (✉)

[1] Department of Materials Science and Engineering, College of Engineering, Peking University, Beijing 100871, China
[2] Department of Radiology, Affiliated Hospital of the Academy of Military Medical Sciences, Beijing 100071, China

Received: 24 May 2012 / Revised: 18 July 2012 / Accepted: 13 August 2012

ABSTRACT

Multifunctional probes for simultaneous magnetic resonance imaging (MRI) and drug delivery have attracted considerable interest due to their promising potential applications in the early-stage diagnosis and therapy of the diseases. In this study, hollow manganese phosphate nanoparticles (HMP NPs) with an average diameter of 18 nm were synthesized and aminated through silanization, which enabled the covalent conjugation of biocompatible poly(ethylene glycol) (PEG) on their surfaces. The anti-tumor drug doxorubicin (DOX) could be loaded into the hollow cavities. Under physiological conditions (pH 7.4), the NPs showed low MRI T_1 contrast (r_1 = 1.19 L·mmol^{-1}·s^{-1}), whereas high T_1 enhancement (r_1 = 5.22 L·mmol^{-1}·s^{-1}) was achieved after dissolving them in endosome/lysosome mimetic conditions (pH 5.4). This is due to the fact that the NPs were easily eroded, which resulted in the release of Mn^{2+} at low pH. To use this interesting phenomenon for targeted DOX drug delivery, we conjugated the tumor-targeting ligand folic acid (FA) on HMP NPs and investigated their drug delivery capacity and cytotoxicity to cell lines expressing different amount of folate receptor (FR). KB cells showed more significant cellular uptake than HeLa cells and A549 cells, as confirmed by confocal laser scanning microscopy (CLSM), flow cytometry and cellular T_1-weighted MRI. Furthermore, the drug-loaded HMP NPs exhibited greater cytotoxicity to KB cells. Our results suggest that functionalized HMP NPs can act as an effective multifunctional probe for selective diagnosis with MRI, as well as giving efficient targeted drug delivery.

KEYWORDS

Manganese phosphate, molecular probe, magnetic resonance imaging (MRI), targeted drug delivery

1. Introduction

Magnetic resonance imaging (MRI) is one of the most powerful and versatile imaging techniques in both clinical and research settings, and has provided high spatial resolution combined with excellent anatomical details of soft tissues without usage of radioisotopes [1, 2]. The introduction of contrast agents accelerates the relaxivity of water, and thereby, greatly improves the MRI sensitivity and contrast effect. The most commonly employed MRI contrast agent in the clinic is a paramagnetic gadolinium-based complex, however, its extensive application is limited by the toxicity of Gd^{3+} and the short circulation half-life time. Considering

Address correspondence to Yanglong Hou, hou@pku.edu.cn; Fugeng Sheng, shengfugeng@gmail.com

their lower toxicity and presence of five unpaired electrons, manganese-based contrast agents have been approved as a clinical agent.

In recent years, nanoparticles (NPs) with controlled phase, shape, and size have been extensively used in biomedical applications for imaging, drug delivery, and gene therapy [3–7]. Although magnetic NPs such as MFe_2O_4 (M = Fe, Co, Mn) NPs have attracted considerable research interest due to their unique magnetic and electrical properties [8–10], they are negative imaging agents which provide dark signal and may lead to misdiagnosis, as the signal is often confused with bleeding, calcification or metal deposits [11, 12]. Very recently, other manganese-based NPs have shown great potential due to their positive contrast ability and relatively low toxicity [11, 13–16].

For an ideal MRI contrast agent, high relaxivity is essential in order to reduce the amount of agent required, resulting in lower toxicity [17]. However, compared with Mn^{2+} or Gd^{3+} chelates, the r_1 relaxivity of manganese-based NPs is relatively low, owing to the absence of water coordinated with Mn^{2+}. To enlarge the water-accessible surface, hollow structures have been introduced, which increased the r_1 relaxivity from 0.209 $L{\cdot}mmol^{-1}{\cdot}s^{-1}$ to 1.417 $L{\cdot}mmol^{-1}{\cdot}s^{-1}$ [18, 19]. In addition, the hollow cavities in NPs are available for drug or gene delivery [20–22]. Therefore, hollow manganese-based NPs would be a good candidate as a multifunctional probe for MRI and drug delivery.

One of the biggest remaining challenges in tumor diagnosis and treatment is how to distinguish the tumor from normal cellular tissue and selectively release drugs at the target site. One of the effective ways to solve this problem is pH-sensitive release. It has been reported that the tumor extracellular environment is more acidic (pH 6.5) than blood or normal tissues (pH 7.4), and the pH values of endosomes and lysosomes are even lower at 5.0–5.5 [23, 24]. Therefore, targeted drug delivery has been realized by using pH-sensitive materials [25–27]. In addition, it has been shown that manganese oxides or manganese carbonates will gradually dissolve in an acidic environment and release Mn^{2+}, which results in a dramatic enhancement of the brightness in T_1-weighed MRI compared with that under normal conditions [28, 29]. Thus, MRI-based cell tracking for diagnosis can be achieved by taking advantage of the pH difference between intracellular and extracellular environments. However, the manganese-based materials reported for MRI have usually been in a crystalline form, and therefore, show reduced sensitivity to pH. In contrast, we have previously synthesized hollow manganese phosphate nanoparticles (HMP NPs) which are amorphous, and can therefore respond to the pH value much faster and release more Mn^{2+} than other manganese-based materials. Therefore the goal of rapid tumor diagnosis and therapy can be easily accomplished as long as the probe can specifically bind to the tumor site. Fortunately, cancer cell targeting can be achieved by means of conjugation of specific ligands to the probe. Folic acid (FA) has been widely used as a ligand because the folate receptor (FR) is overexpressed in many types of cancer cells but is absent in normal tissues [30, 31]. Therefore, FA-mediated delivery should be an effective way for tumor-only theranostics.

Here, we design a novel multifunctional probe utilizing amorphous HMP NPs modified with 3-aminopropyltriethoxysilane (APS), polyethylene glycol (PEG) and FA for MRI-based targeted diagnosis and drug delivery, as schematically depicted in Scheme 1. Functionalized pH-sensitive HMP NPs possess the following advantages: (1) Extremely high MRI T_1 enhancement at tumor sites compared with traditional manganese-based NPs based on the high sensitivity of HMP NPs to pH value and high relaxivity arising from rapidly released Mn^{2+}; (2) low MRI signal at normal sites resulting from the stability of HMP NPs under physiological conditions; (3) tumor-targeted drug delivery capacity for tumor treatment with fewer side effects due to the targeting modification. As a result of the hollow structure and dissolution of HMP NPs releasing Mn^{2+} under acid conditions, this probe exhibits high drug loading efficiency, and pH-selective MR imaging and drug release capacities. The T_1- and T_2-weighted images showed much higher performance than traditional manganese-based NPs, and FA conjugation enabled them to be selectively recognized by target cells, which enhanced the local cytotoxicity and T_1-based MRI signal at sites of interest.

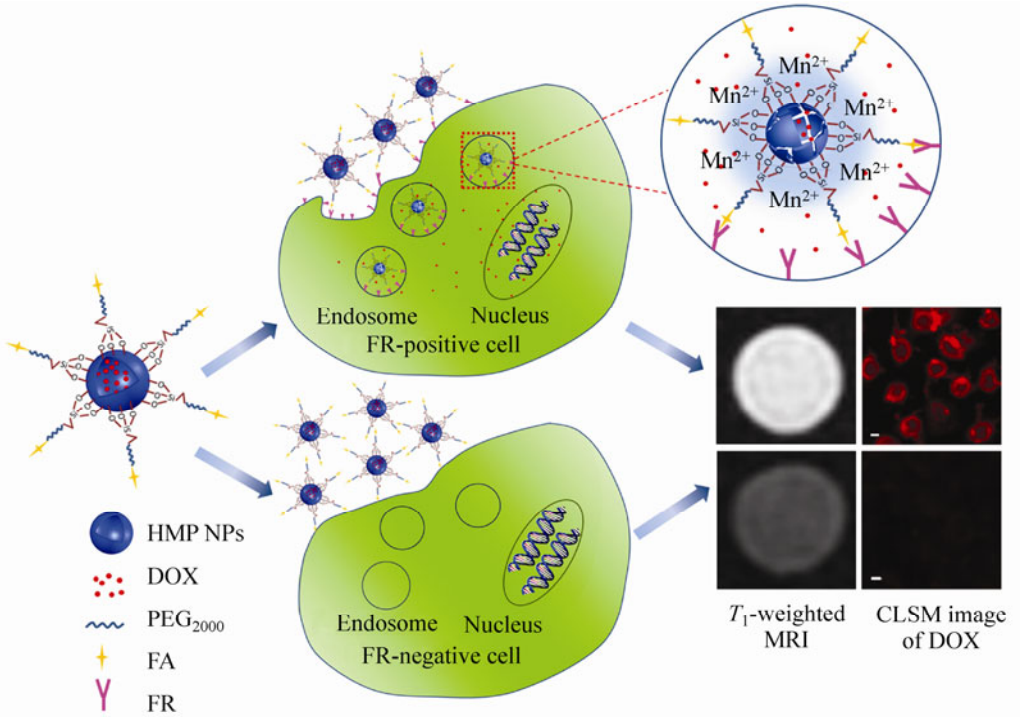

Scheme 1 Schematic illustration of the concept for FR-mediated intracellular uptake of DOX-loaded HMP NPs for selective MRI and drug delivery

2. Experimental

2.1 Materials

Triethyl phosphate (97%, Alfa Aesar), manganese(Ⅱ) acetylacetonate ($Mn(acac)_2$ Alfa Aesar), oleylamine (OAm, 99%, China Resources (Boxing) Oleochemicals Co. Ltd.), oleic acid (OA, 90%, Alfa Aesar), *N*,*N*′-dicyclohexylcarbodiimide (DCC, 99%, Alfa Aesar), *N*-hydroxysuccinimide (NHS, 98+%, Alfa Aesar), APS (97%, Beijing Xindingpengfei Science and Technology Co. Ltd), polyethylene glycol diacid (PEG diacid, M_w. 2000, 97%, Beijing Kaizheng Biotech Development Co. Ltd), folic acid (FA, 96%, J&K Scientific), phosphate buffer solution (PBS, Beijing Solarbio Science and Technology Co. Ltd), doxorubicin hydrochloride (DOX·HCl, 98%, Beijing Huafeng United Technology Co. Ltd) were used as supplied. All other chemicals were purchased from China National Medicines Co. Ltd. and were of analytical purity and used without further purification. Deionized water was employed in all experiments.

2.2 Synthesis of HMP NPs

The HMP NPs were prepared following our previously reported method [32] with slight modifications. Briefly, 1 mL of OA and 4 mL of OAm were dissolved in 15 mL of toluene in a 25 mL Teflon-lined autoclave, and then 0.2 mL of deionized water, 0.4 mL of triethyl phosphate, and 1 mmol of $Mn(acac)_2$ were added into the solution under stirring. The autoclave was sealed and placed in an oven at 180 ℃ for 9 h. The dispersion was precipitated with ethanol and separated by centrifugation, followed by re-dispersing in hexane and standing overnight. The upper solution containing the product was collected for further use. To synthesize solid manganese phosphate nanoparticles (SMP NPs), the reaction time was changed to 5 h with the other conditions remaining unchanged.

2.3 Preparation of silane-modified HMP NPs (HMP–APS NPs)

To transfer HMP NPs into water, APS was introduced with a ligand exchange method following a literature procedure [33]. 100 μL of APS was added to a dispersion of hydrophobic HMP NPs in hexane (10 mg in 30 mL) containing 0.01% (*v*/*v*) acetic acid. The mixture was shaken for 72 h at room temperature, during which the solution became milky. The white colored product

was collected using centrifugation (20 000 r/min) and washed twice with hexane, ethanol and water to remove unmodified NPs and extra APS, and then lyophilized and stored at 4 ℃ for further use.

2.4 Synthesis of PEGylated APS (APS–PEG–COOH)

To inhibit plasma coating on NPs and allow escape from the reticuloendothelial system (RES) for longer circulation times, PEG was introduced through a covalent bond via DCC/NHS chemistry. 100 mg of PEG diacid, 6.5 mg of NHS and 4.2 mg of DCC were dissolved in a mixture of 7.5 mL of dimethyl sulfoxide (DMSO) and 2.5 mL of $CHCl_3$, containing 40 mg of anhydrous Na_2CO_3. The solution was stirred at room temperature for 2 h before 12 μL of APS in 5 mL of $CHCl_3$ were added, and the mixture was further stirred at room temperature under Ar protection for 24 h. The product was collected by centrifugation, washed with DMSO and dialyzed (molecular weight cutoff (MWCO) = 2000), followed by lyophilization before further modification.

2.5 Synthesis of FA conjugated APS–PEG–COOH (APS–PEG–FA)

To improve the targeting of the NPs, FA was conjugated on APS–PEG–COOH via DCC/NHS chemistry. 50 mg of APS–PEG–COOH, 6.5 mg of DCC, 4.2 mg of NHS, and 40 mg of Na_2CO_3 were dissolved in a mixture of 10 mL of DMSO and 5 mL of $CHCl_3$, and stirred under Ar at room temperature for 2 h. 12 mg of FA dissolved in 15 mL of DMSO were added to the activated APS–PEG–COOH solution, and the mixture was stirred gently for another 24 h at room temperature under Ar protection. APS–PEG–FA was purified by centrifugation, washed with DMSO and dialyzed (MWCO = 2000), then lyophilized and stored at 4 ℃ before using.

2.6 Preparation of PEGylated HMP NPs (HMP–PEG NPs)/FA modified HMP NPs (HMP–FA NPs)

10 mg of HMP–APS NPs and 20 mg of APS–PEG–COOH/APS–PEG–FA were mixed in 10 mL of DMSO, and stirred under Ar protection for 24 h. The products were collected by centrifugation followed by washing with DMSO and water, and then dispersed in water and remove free PEG diacid or APS–PEG–FA by dialysis (MWCO = 10 000) for 24 h in water. The product was then lyophilized and stored at 4 ℃ for further use.

2.7 Loading DOX in HMP–PEG/HMP–FA NPs (HMP–DOX/HMP–FA–DOX NPs)

Loading of the anti-tumor drug DOX into HMP–PEG NPs was achieved by mixing DOX (with varying concentrations from 0.25 mmol/L to 3 mmol/L) with HMP–PEG NPs (with a manganese concentration of 90 $\mu g \cdot mL^{-1}$) in PBS (with pH of 7.0 or 8.0) overnight. Free DOX was removed by centrifugation at 20 000 r/min and washing three times with PBS. Loading of DOX on HMP–FA NPs and PEGylated SMP NPs (SMP–PEG NPs) was carried out by the same process with the same amount of initial DOX and Mn^{2+}. The amount of DOX incorporated into HMP NPs was determined by the absorbance at about 500 nm after subtracting the absorbance contributed by HMP NPs at the same wavelength, similar to the measurement of DOX loading on functionalized single walled carbon nanotubes [34, 35].

2.8 DOX releasing efficiency of HMP–DOX/HMP–FA–DOX NPs

HMP–DOX was re-dispersed in $NaHCO_3/Na_2CO_3$ buffer at pH 5.4 or PBS at pH 7.4, and shaken gently at room temperature in the dark for different periods of time. HMP–DOX was centrifuged at 15 000 r/min for 10 min. The amount of released DOX in the supernatant solution was measured by UV–vis absorbance spectroscopy.

2.9 Characterization techniques

Electron micrographs were obtained using a transmission electron microscope (TEM, Tecnai G2 T20, FEI, USA, at 200 kV). X-ray diffraction (XRD) patterns were recorded on a Philips X'Pert Pro diffractometer with Cu Kα (λ = 1.5405 Å) radiation. IR spectra were measured using a KBr disk in a Fourier transform infrared (FTIR) spectrometer (Vector 22, Nicolet, USA). Thermogravimetric analysis (TGA) was recorded on Q50TGA instrument (Thermal Analysis, USA). Dynamic light scattering (DLS) was measured using

a particle size analyzer (ZetaPALS, Brookhaven Instruments, Holtsville, NY). Loading and release of DOX from HMP–DOX were quantified using a UV–vis spectrophotometer (UV2550, Shimadzu, Japan) using the absorbance peak at λ = 480 nm. The concentrations of Mn^{2+} were quantified using an inductively coupled plasma–atomic emission spectrometer (ICP–AES, Profile, Leeman, USA).

2.10 Measurement of MRI relaxation properties

T_1 and T_2 relaxation of the HMP NPs in pH 5.4 and pH 7.4 were measured in test tubes with a 1.5T clinical MRI scanner (Signa EXCITE HD 1.5T TwinSpeed system, General Electric Company, USA). HMP NPs at pH 5.4 with various concentrations of manganese (0–1.00 mmol/L) were dispersed in NaAc/HAc buffer solution, and pH 7.4 PBS. MR images were acquired using a T_1-weighted sequence with the following parameters: Repetition time (TR) = 300, 350, 400, 450, 500, 550, 600, 650 ms, echo time (TE) = 11 ms, matrix size = 256 × 256, field of view (FOV) = 120 × 120 mm^2, slice thickness = 2 mm, number of excitations (NEX) = 1. The parameters of a T_2-weighted sequence were as follows: TR = 3000 ms, TE = 0, 30, 40, 60, 80, 100, 120, 140 ms, matrix size = 256 × 256, FOV = 120 × 120 mm^2, slice thickness = 2 mm, NEX = 1. All post-processings were performed on the GE ADW 4.3 workstation. T_1-mapping and T_2-mapping images were acquired by using the post-processing software in Functool, and the selected region of interests (ROIs) in the T_1-mapping and T_2-mapping were measured with the same size to obtain the signal intensities for each concentration. Based on the inverse relaxation time ($1/T_1$) and ($1/T_2$), the resulting r_1 and r_2 values were measured as a function of Mn^{2+} concentration.

2.11 Cell culture

A human nasopharyngeal epidermal carcinoma cell line (KB cells), a human cervical carcinoma cell line (HeLa cells), and a human lung adenocarcinoma epithelial cell line (A549 cells) were obtained from Cancer Institute and Hospital Chinese Academy of Medical Science. All cell culture related reagents were purchased from Invitrogen. Cells were cultured in normal RPMI-1640 culture medium supplemented with 10% fetal bovine serum (FBS) and 1% penicillin/streptomycin at 37 ℃ under 5% CO_2. Cells were plated in tissue culture flasks under 100% humidity. All NPs were sterilized by filtration through a 0.22 μm filter before incubation with cells.

2.12 Cytotoxicity by 3-(4,5-dimethylthiazol-2-yl)-2,5-diphenyl tetrazolium bromide (MTT) assay

The *in vitro* cytotoxicity of HMP and HMP–FA NPs was evaluated using a standard MTT assay on KB cells, HeLa cells, and A549 cells. All cells were seeded into 96-well cell culture plates at 5 × 10^3 per well and incubated overnight at 37 ℃ under 5% CO_2. After removing the culture medium, various concentrations of HMP–PEG and HMP–FA in culture medium were added, followed by further incubation for 24 h. The OD570 value (Abs.) of each well was measured by a luminescence microplate reader (SpectraMax M2, Molecular Device, USA). The cytotoxicity of drug-loaded NPs to KB cells, HeLa cells, and A549 cells was carried out for free DOX, HMP–DOX, and HMP–FA–DOX (with the same amount of DOX) in the same way with the maximum manganese concentration of 0.3 mmol/L. To evaluate the targeting ability, cells were pretreated with excess free FA for 1 h before incubation with HMP–FA–DOX.

2.13 Cellular uptake measured by confocal laser scanning microscopy

KB cells were seeded at a density of 1 × 10^5 cells per well on a glass cover in a 24-well cell culture plate. After incubation at 37 ℃ under 5% CO_2 overnight, the medium was carefully aspirated, and replaced by culture medium with HMP–DOX and HMP–FA–DOX, at a DOX concentration of 10 μmol/L for 2 h. In a free FA competition study, FA was added to the culture medium at a concentration of 4 mmol/L and the mixture subjected to a pre-incubation for 1 h before adding HMP–FA–DOX. After incubation, cells were washed three times with 1 mL of Dulbecco's phosphate buffered saline (DPBS) and fixed with 1 mL of 4% paraformaldehyde for 15 min. Nuclei were stained using 4′,6-diamidino-2-phenylindole (DAPI). To investigate the colocalization of DOX and lysosomes, cells were stained with 1 mmol/L Hoechst 33342 (Invitrogen)

for 20 min and 1 mmol/L LysoTracker Green DND-26 (Invitrogen) for 5 min after incubation with HMP–FA–DOX NPs for 2 h, then washed three times with DPBS and transferred to the culture medium. Cells were imaged by using confocal laser scanning microscopy (Zeiss Axio Observer A1, Germany) under laser excitation at 488 nm (for DOX), 364 nm (for DAPI or Hoechst 33342), and 515 nm (for LysoTracker). HeLa cells and A549 cells incubated with HMP–FA–DOX were carried out under the same conditions.

2.14 Flow cytometry

Flow cytometry was used to further quantify the FA-receptor specificity of NPs phagocytosed by KB cells. KB cells were plated at a density of 1×10^5 cells per well in a 24-well cell culture plate (A_1 to E_4) and incubated overnight. After removing the supernatant and washing three times with DPBS, HMP–DOX and HMP–FA–DOX NPs (1 mL in culture medium, containing 10 μmol/L DOX) was added to four of the wells (A_1 to A_4 and B_1 to B_4, respectively) and incubated for 2 h. For a comparative study of FA competition, free FA (200 μL in DPBS, 4 mmol/L) was previously added to four of the wells (C_1 to C_4) and incubated for 1 h, followed by washing three times with DPBS. Then, HMP–FA–DOX with the same amount of DOX was added to the wells and incubated for another 2 h. 10 μmol/L of free DOX was used as a contrast (D_1 to D_4) and KB cells treated with DOX-free HMP–FA NPs were used as a control (E_1 to E_4). After incubation, cells were washed three times with DPBS, trypsinized and re-suspended in DPBS. Finally, a total of 10 000 cells per sample were analyzed using a flow cytometer (MoFlo, Cytomation, USA). For detection of DOX-derived fluorescence, excitation was conducted with a 488 nm argon laser, and fluorescence emission at 575 nm was measured.

2.15 *In vitro* MR imaging

KB cells, HeLa cells, A549 cells and FA-saturated KB cells with a density of 1×10^6 cells per well were cultured in 6-well culture plates overnight before being treated with HMP–FA–DOX NPs, with varying Mn^{2+} concentration (from 25.4 μg·mL^{-1} to 5.08 μg·mL^{-1}). After washing three times with DPBS, cells were trypsinized and suspended in 1 mL of DPBS before measuring MRI at 1.5 T. Inductively coupled plasma atomic emission spectroscopy (ICP–AES) was used to measure the manganese concentration in cells.

3. Results and discussion

3.1 Preparation of HMP NPs

HMP NPs were prepared by our previously reported procedure [32] with a slight modification. The average size of the as-prepared HMP NPs was about 18 nm with a 10 nm core, as characterized by TEM (Fig. 1(a)), and further confirmed by DLS (Fig. 1(c)). With the aid of OA and OAm, HMP NPs can be well dispersed in hexane, as shown in the inset of Fig. 1(a). XRD analysis showed that the NPs were amorphous but were transformed into crystalline monoclinic $Mn_3(PO_4)_2$ (JCPDS 31-0827) after annealing at 500 °C for 2 h (Fig. S-1(a) in the Electronic Supplementary Material (ESM)). After annealing, the hollow structures of HMP NPs collapsed, and particles aggregated, as shown in Fig. S-1(b) (in the ESM). To make full use of the hollow structure, the as-prepared HMP NPs without annealing were selected for further application.

APS was introduced to transform the hydrophobic NPs into water soluble ones. After surfactant exchange, HMP NPs could be well-dispersed in water and the dispersion remained stable for at least 1 month (Fig. 1(b)) without any change of particle morphology. Figure 1(d) shows DLS measurements for HMP–APS NPs. The hydrodynamic size increased to 40–60 nm, which may indicate the tendency of NPs to aggregate into dimers or trimers. In order to give longer circulation times and enhance the FA-targeting effect, PEG modification and FA conjugation were introduced. The successful modification was confirmed by FTIR and TGA (Figs. S-2 and S-3 (in the ESM)).

3.2 Drug loading and release efficiency

Due to the hollow structure of HMP NPs, we hypothesized that drugs could be loaded in the hollow parts for potential drug delivery with high efficiency. To prove this point, HMP–APS NPs and APS-modified solid manganese phosphate NPs

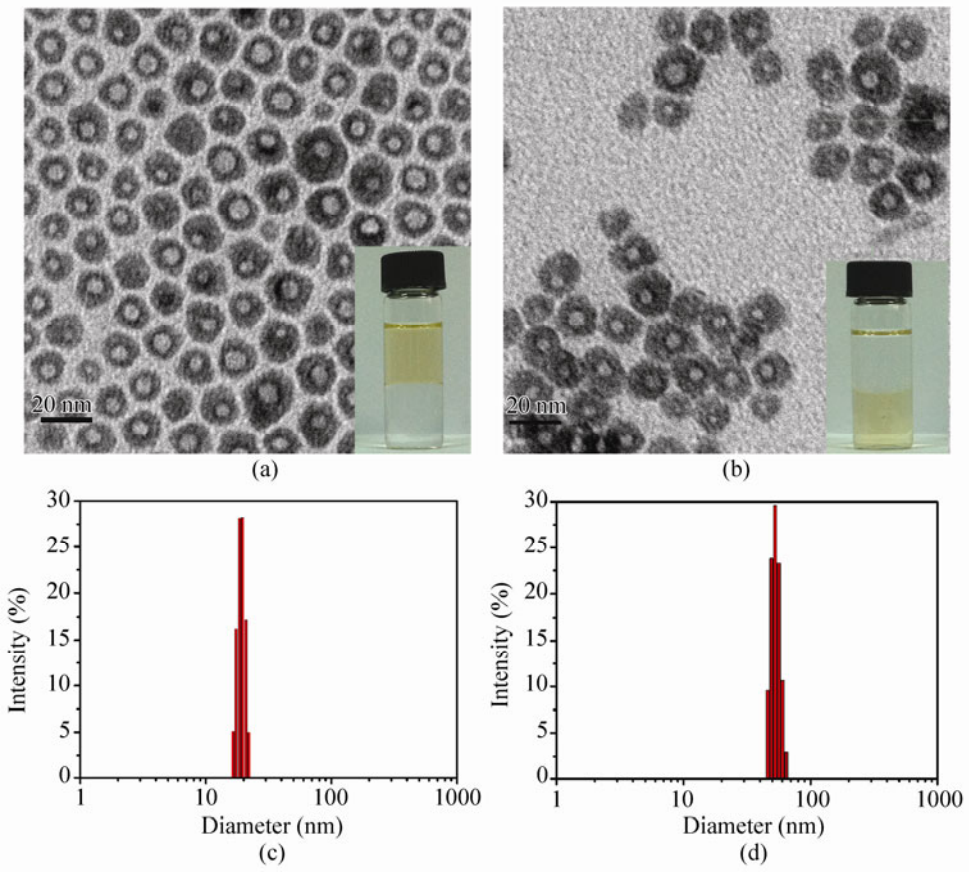

Figure 1 TEM images of (a) HMP NPs and (b) APS-modified HMP NPs. Insets are the photographs of hexane soluble HMP NPs and water soluble APS-modified HMP NPs, respectively. Hydrodynamic size distribution of (c) HMP NPs and (d) APS-modified HMP NPs monitored by DLS

(SMP–APS NPs) were stirred with various amounts of hydrophilic DOX·HCl in the dark overnight at pH 7. The method used to determine the amount of DOX in HMP–DOX NPs and SMP–DOX NPs was similar to that used to measure the DOX loading on carbon nanotubes [34], i.e. measuring the absorbance at about 500 nm (Fig. 2(a), red and blue lines). The slight change of the peak position compared to free DOX (Fig. 2(c), blue line, about 480 nm) was attributed to the interaction of DOX with NPs, which provides preliminarily evidence of the loading of DOX into NPs. Based on the concentration of Mn^{2+}, the loading capacity of HMP NPs at pH 7 was about 20% (Fig. 2(b), red), close to double that of SMP NPs (Fig. 2(b), blue), due to the larger surface area resulting from the hollow structure. However, when HMP–APS and SMP–APS NPs were mixed with various amounts of DOX·HCl at pH 8, under which condition DOX·HCl was deprotonated to become hydrophobic [35], the loading capacity of HMP-APS NPs reached 30% (Fig. 2(b), black), almost three times that of SMP-APS NPs (Fig. 2(b), magenta) at the same pH, and 1.5 times that of HMP-APS NPs at pH 7.0. The increase in the loading capacity of HMP-APS may be attributed to the hydrophobic interactions between DOX and OA or OAm remaining in the inner cavity [19], as well as the influence of the larger surface area, further suggesting that DOX was loaded into the hollow part under these conditions. The loading capacities of SMP-APS NPs at pH 7 and 8 (Fig. 2(b), blue and magenta) were almost the same, suggesting a similar interaction under these two conditions due to the equivalent available surface areas. Furthermore, if the HMP NPs were annealed at 500 ℃, the loading capacity decreased severely at pH values of both 7 and 8 (Fig. S-4 (in the ESM), red and blue lines), and became even lower

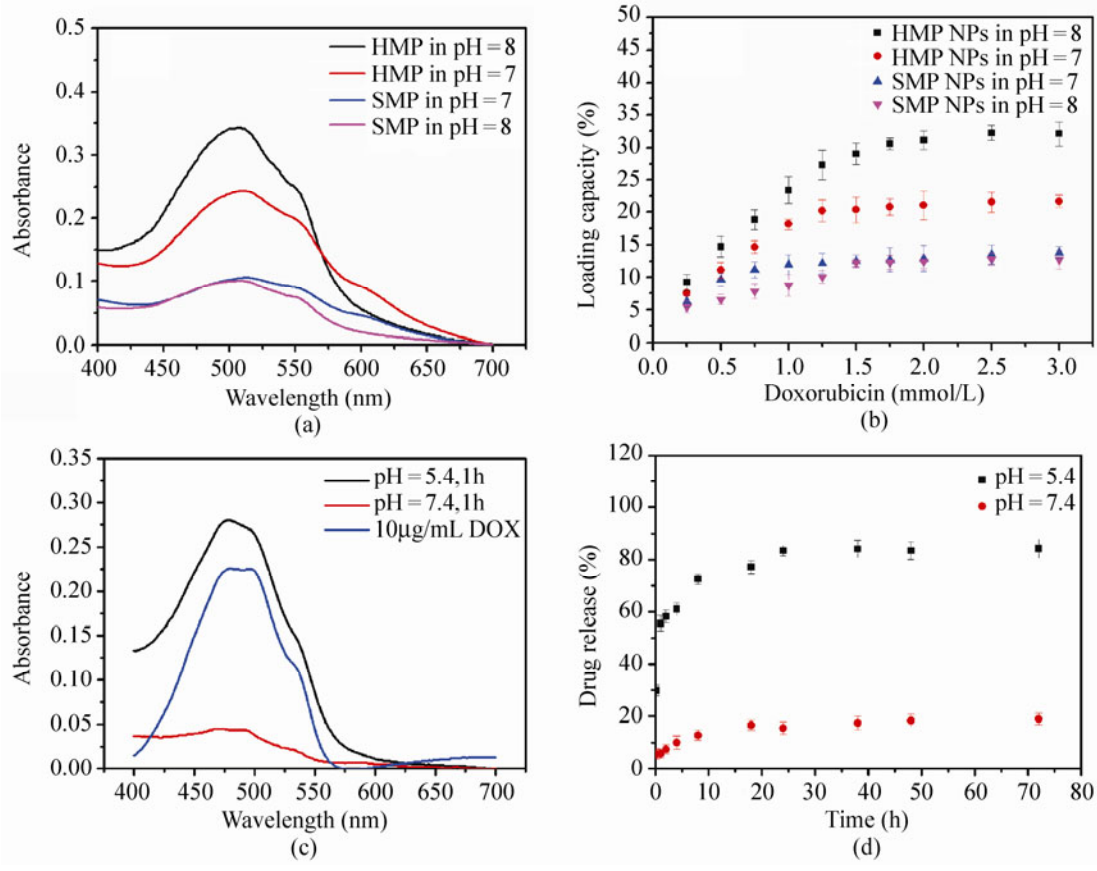

Figure 2 (a) UV–vis absorbance spectra of HMP NPs and SMP NPs loaded with 1.5 mmol/L DOX at pH 7 and pH 8 with the same manganese concentration (1.2 mmol/L). Solutions were diluted eight times before testing. (b) Quantification of DOX loading capacity of HMP NPs and SMP NPs at different DOX concentrations at pH 7 and pH 8. Error bars are based on standard deviations of triplicated samples. (c) UV–vis absorbance spectra of 10 $\mu g \cdot mL^{-1}$ free DOX and DOX released from HMP–DOX NPs at pH 7.4 and pH 5.4 for 1 h. HMP–DOX NPs were loaded with 0.24 mmol/L DOX and DOX released was diluted ten times before testing. (d) Quantification of DOX releasing efficiency of HMP NPs at different times at pH 5.4 and pH 7.4. Error bars are based on standard deviations of triplicated samples

than that of SMP NPs. This can be ascribed to the hollow structure of HMP NPs being broken down followed by aggregation during the annealing process, resulting in a dramatic decrease in the surface area. Therefore, we can conclude that the as-synthesized HMP NPs may be a good candidate for drug delivery, especially for hydrophobic drugs.

Drugs loaded in NPs should be released under specific conditions for an ideal drug delivery system. For tumor-targeting delivery, some specific release mechanisms have been considered due to the specific environment of tumors, such as pH [23, 36], enzymatic interactions [37, 38], and reducing environment [39, 40]. Of these, pH-controlled release is one of most promising routes because of its manipulability and wide applicability. The pH-sensitive drug release behavior of HMP–DOX was demonstrated under various pH conditions (Figs. 2(c) and 2(d)). At pH 5.4, a saturated DOX release efficiency of almost 90% was achieved within 72 h, while only 15% was reached at pH 7.4. Compared to some traditional pH-sensitive materials [21, 41], the susceptibility to pH of HMP–DOX is superior, making it more accurate in pH-selective drug release systems. This is because traditional pH-sensitive drug release properties are affected by the protonation of DOX in acid conditions, which weakens the interactions of DOX with the surfactant, triggering release of the drug [35]. However, in the DOX-loaded HMP NPs system, the rapid response of HMP NPs in acid conditions may also

greatly contribute to the controlled release of the drug by causing cracking of the hollow structure. To confirm this hypothesis, TEM and DLS characterization were carried out by dispersing HMP NPs in pH 5.4 and pH 7.4 buffer. HMP NPs cracked into small pieces with particle sizes much smaller than 10 nm at pH 5.4 (Fig. S-5(a) in the ESM), while the morphology was well-maintained at pH 7.4 (Fig. S-5(b) in the ESM). DLS analysis further confirmed this result, as the diameter distribution shifted to 3–5 nm at pH 5.4 (Fig. S-5(c) in the ESM), lower than that at pH 7.4 (Fig. S-5(d) in the ESM). From these observations, we can conclude that this pH susceptibility can accelerate drug release at the tumor site, which highlights the potential of HMP NPs as a vehicle for drug delivery.

3.3 Measurement of MR relaxation properties

To examine the MR relaxation properties of HMP NPs as a contrast agent, the longitudinal relaxation rate ($r_1 = 1/T_1$) and transverse relaxation rate ($r_2 = 1/T_2$) arising from the concentration of Mn^{2+} released in pH 5.4 and pH 7.4 buffer were assayed using a 1.5 T human clinical scanner. Interestingly, the HMP NPs dispersed in pH 5.4 buffer displayed a much stronger enhancement in both T_1- and T_2-weighted MRI than in pH 7.4 buffer (Fig. 3). The r_1 and r_2 values at pH 5.4 were 5.52 L·mmol^{-1}·s^{-1} and 23.40 L·mmol^{-1}·s^{-1}, which are respectively 3.70 and 1.47 times higher than the values at pH 7.4. At pH 5.4, both r_1 and r_2 relaxivity are significantly higher than those previously reported for manganese-based contrast agents [11, 13–16]. The pH-sensitivity of HMP NPs should be the critical cause of this interesting phenomenon. It can be assumed that when HMP NPs were eroded, the released Mn^{2+} will improve the contrast ability [28, 29]. To confirm this assumption, the HMP NPs were dispersed in buffer solutions of pH 7.4 and pH 5.4, followed by centrifugation at 15 000 r/min for 30 min. The manganese concentrations in the supernatant and sediment were measured. As shown in Fig. S-6(a) (in the ESM), 97% of Mn^{2+} ions remained in the supernatant at pH 5.4, while only 4% of Mn^{2+} ions remained at pH

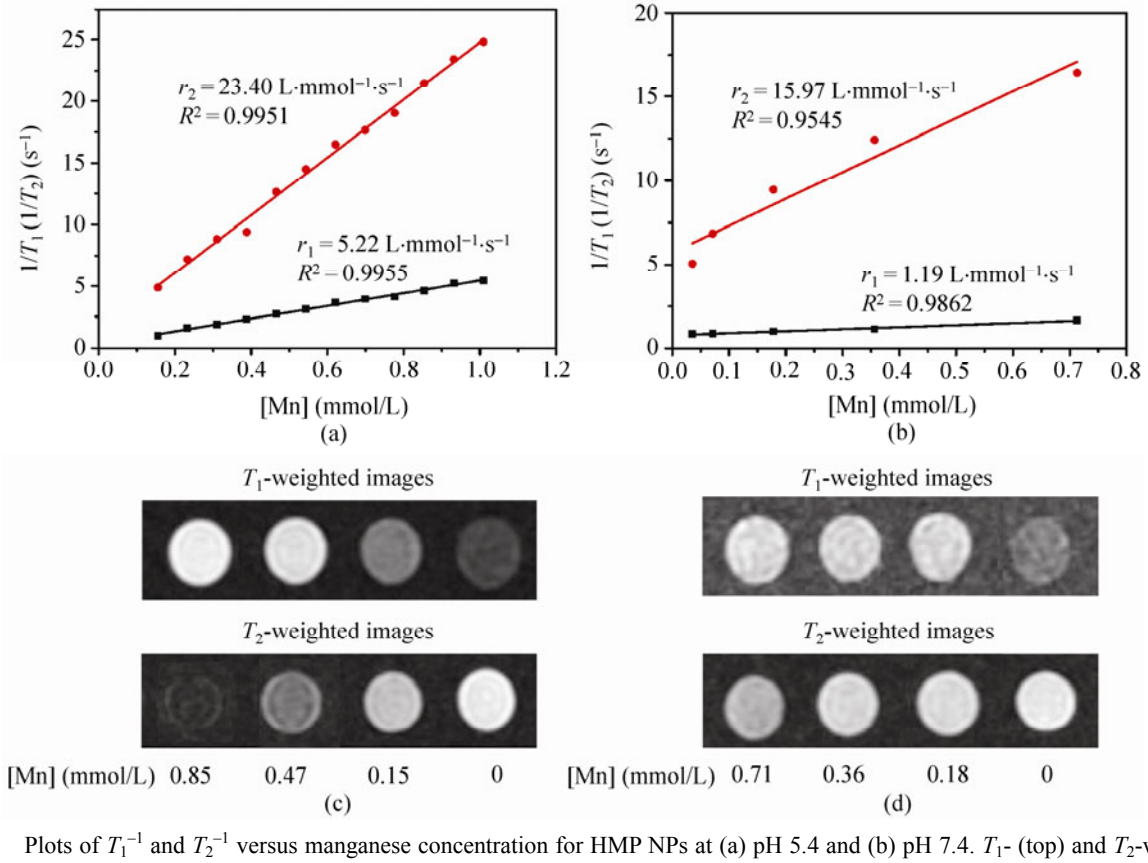

Figure 3 Plots of T_1^{-1} and T_2^{-1} versus manganese concentration for HMP NPs at (a) pH 5.4 and (b) pH 7.4. T_1- (top) and T_2-weighted (bottom) images of HMP NPs at (c) pH 5.4 and (d) pH 7.4 in a 1.5 T MRI system

7.4, suggesting that HMP NPs were mostly dissolved giving Mn^{2+} at low pH, but very stable at high pH. In addition, the stability of HMP NPs at neutral pH prohibited Mn^{2+} from dissociating allowing the suspension to be stable for at least for l month (Fig. S-6(b) in the ESM), which demonstrates that the probe is stable in a physiological environment. The relaxation properties of $MnCl_2$ were evaluated under the same conditions (Fig. S-7 in the ESM) and showed both similar T_1 enhancement and T_2 contrast effect to that of HMP NPs at pH 5.4. Remarkably, the r_1 and r_2 values of $MnCl_2$, 5.73 $L{\cdot}mmol^{-1}{\cdot}s^{-1}$ and 27.20 $L{\cdot}mmol^{-1}{\cdot}s^{-1}$, were only slightly larger than the values for HMP NPs at pH 5.4, which provides further evidence that ~95% of HMP NPs dissolved to give Mn^{2+} at pH 5.4. When HMP NPs were annealed at 500 ˚C, as the crystallinity increased, the pH-sensitivity decreased. As demonstrated in Fig. S-8 (in the ESM), only 60% of the annealed NPs were eroded into Mn^{2+} at pH 5.4, and it took at least 12 h to reach the maximum releasing point, compared with 97% Mn^{2+} release from non-annealed NPs within 2 h. As discussed above, the ability of pH-selective MRI contrast is related to the pH-responsive property of HMP NPs, and consequently, the lower amount of Mn^{2+} released and longer release time required for annealed HMP NPs would result in lower contrast in MRI. As a result, the pH-convertible MRI contrast property for HMP NPs enabled the probe to be a better MRI contrast agent for cellular tracking with high sensitivity, especially at tumor sites with lower pH value.

3.4 Targeting drug delivery and cytotoxicity assay

The toxicity of a probe without any drug loading is an important consideration for a delivery system. To evaluate the cytotoxicity of HMP NPs, KB cells, HeLa cells, and A549 cells incubated with HMP NPs were subjected to MTT assay. As shown in Fig. 4(a), relatively high cell viability (more than 75%) was achieved in all cell lines after incubation for 24 h with HMP–PEG NPs, even at very high manganese concentrations of 2.40 mmol/L. Furthermore, the cell viability of FA-targeted HMP–FA NPs on these three cell lines was assessed (Fig. 4(b)), since it is well known that KB cells strongly overexpress FR (FR++), HeLa cells are FR positive (FR+) and A549 cells are FR negative (FR-) [42, 43]. As expected, the HMP–FA NPs were more cytotoxic to KB cells than HeLa cells, and least cytotoxic to A549 cells. Moreover, compared to the non-targeted HMP–PEG NPs, the HMP–FA NPs had a similar cytotoxicity to A549 cells, but gave much lower cell viability in KB cells. This suggests that the delivery of HMP–FA NPs is through a FR-mediated cellular uptake, and the cytotoxicity arises from free Mn^{2+} released from the HMP NPs [44–46]. Upon entering cells, it is trafficked into endosomes, followed by fusing with lysosomes. The acid conditions in endosomes (pH 5–6) or lysosomes (pH 4–5) cracked the HMP NPs releasing Mn^{2+} [47, 48]. In addition, the action of HMP–FA NPs on FR-passive cells mimics

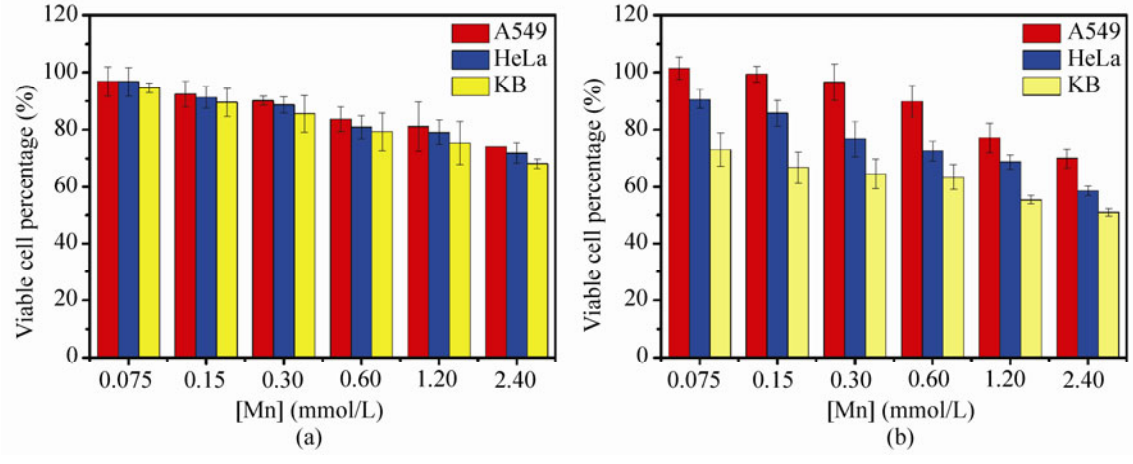

Figure 4 MTT assay of (a) HMP–PEG NPs and (b) HMP–FA NPs on KB cells, HeLa cells, and A549 cells. Error bars are based on standard deviations of six parallel samples

the interaction with normal cells. Despite the risk of cytotoxicity from Mn^{2+}, low uptake efficiency can reduce the toxicity to normal cells. As shown, at low manganese concentrations of HMP–FA NPs, low cytotoxicity was observed in A549 cells. When the manganese concentration was reduced to less than 0.30 mmol/L, little cytotoxicity was observed, indicating high biocompatibility to normal cells. Additionally, HMP NPs were very stable at neutral pH, and did not dissociate into Mn^{2+} at pH 7.4 for at least one month. Therefore, the targeted HMP–FA NPs show great potential for fabricating a probe with high viability to normal cells and toxicity to tumor cells, i.e. high selective release ability of drugs.

Upon loading the anti-tumor drug DOX into NPs, the DOX fluorescence of the HMP–DOX NPs and HMP–FA–DOX NPs allowed the direct visualization of cellular uptake. To confirm the FR-mediated targeted drug delivery, confocal laser scanning microscopy (CLSM) was employed to investigate the cellular uptake of HMP–FA–DOX on KB cells, HeLa cells, and A549 cells. As depicted in Fig. 5, after incubation with

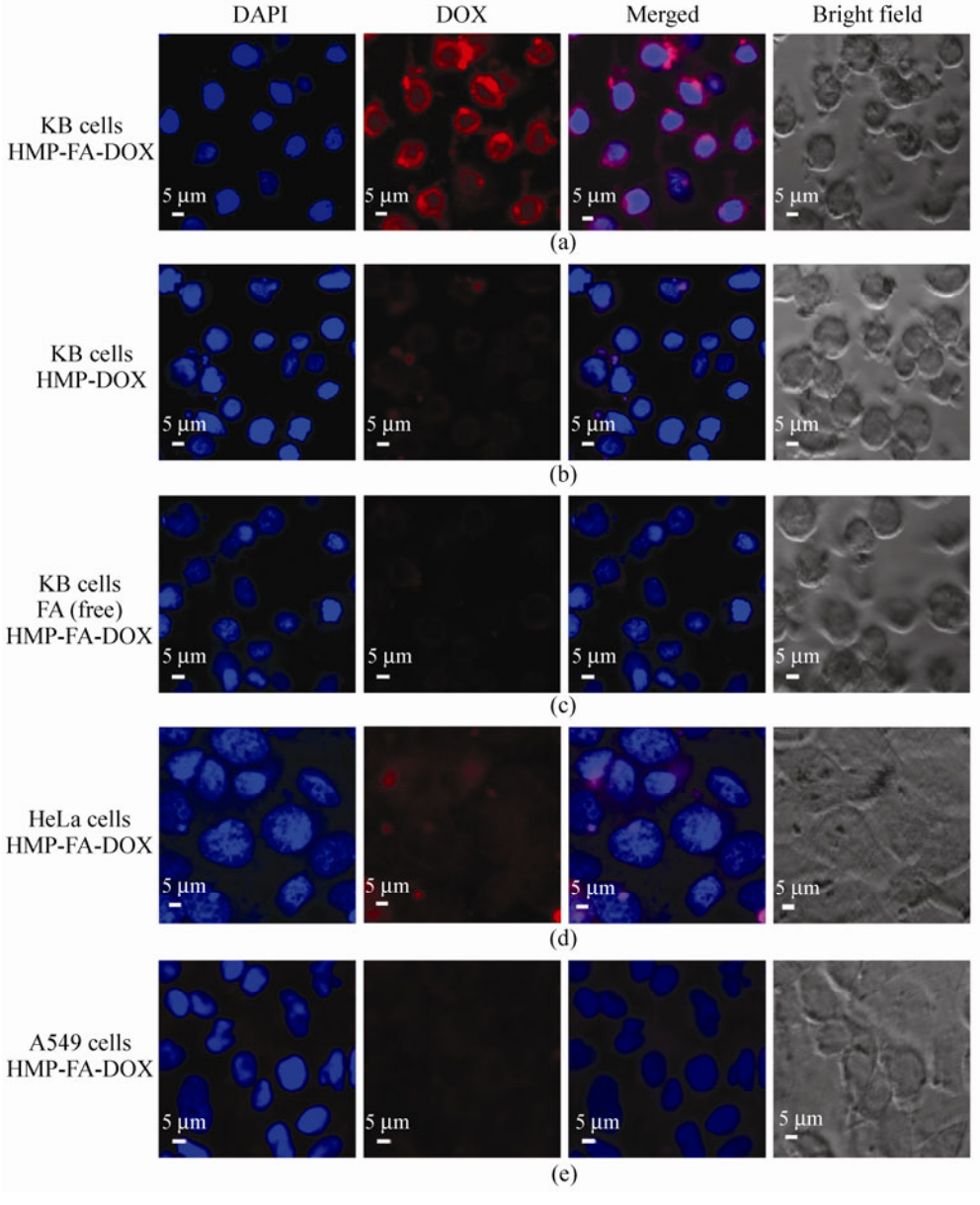

Figure 5 Confocal laser scanning microscopy images of (a) HMP–FA–DOX in KB cells, (b) HMP–DOX in KB cells, (c) HMP–FA–DOX in FA-saturated KB cells, (d) HMP–FA–DOX in HeLa cells, and (e) HMP–FA–DOX in A549 cells. Blue parts are nuclei, stained with DAPI

cells for 2 h, the red fluorescence, which is associated with DOX, was absent in A549 cells, but was visible in HeLa cells and showed considerably higher intensity in KB cells. The fluorescence indicated that the DOX was surrounded closely around the nuclei, implying that DOX was released as the free form, which tends to diffuse towards the nuclei [49]. In contrast, the strong fluorescence in KB cells almost disappeared when it was pre-saturated with a large amount of free FA (4 mmol/L), and negligible fluorescence was observed for HMP–DOX incubated KB cells due to non-specific binding. Moreover, as indicated in Fig. 6, when cells were stained with green fluorescent LysoTracker, the yellow dots, which are a colocalization of a portion of DOX in lysosomes in KB cells, were significantly higher in number and intensity than in A549 cells. When focusing on KB cells, the red fluorescence for DOX in lysosomes was much brighter than that in other organelles in the cytoplasm, suggesting the NPs were mostly in lysosomes. These results confirmed that HMP–FA–DOX NPs were taken up by an FR-mediated mechanism, and the drugs loaded can be mostly released in low pH value lysosomes.

The results of flow cytometry on KB cells (Fig. 7(a)) were in accordance with those of CLSM. HMP–DOX and HMP–FA–DOX with equivalent amounts of DOX (10 μmol/L) were incubated with KB cells for the same time. The cells treated with HMP–FA without DOX were used as a negative control. The mean fluorescence intensity of cells treated with HMP–FA–DOX was 102, while that with the non-targeting HMP–DOX was only 59, thus showing an approximately two-fold improvement in cellular uptake after FA functionalization. When treating KB cells in the presence of excess FA, the fluorescence intensity decreased to 41. The fluorescence intensity of free DOX-treated cells was 191, higher than that for HMP–FA–DOX or HMP–DOX. This can be ascribed to the diffusion of small molecules in the *in vitro* assay being faster than that of NPs [50]. These results directly confirm that the highly FR-specific targeting of HMP–FA–DOX NPs to KB cells involved an FR-mediated endocytosis.

The therapeutic effect of the released drugs on a tumor is another critical factor for a drug delivery system. The anticancer efficacy of HMP–FA–DOX was investigated by the *in vitro* MTT assay against KB cells, HeLa cells, and A549 cells for 24 h, as compared with HMP–DOX, free DOX, and FA-saturated HMP–FA–DOX. To minimize the cytotoxic effect from Mn^{2+}, the drugs were loaded on HMP NPs with the highest manganese concentration of 0.30 mmol/L (with 21.6 μmol/L DOX). As illustrated in Fig. 7(b), compared to HMP–DOX, HMP–FA–DOX exhibited significantly higher growth inhibition levels in KB cells, comparable to free DOX. When HMP–FA–DOX was incubated with FA-containing medium, a much higher cellular

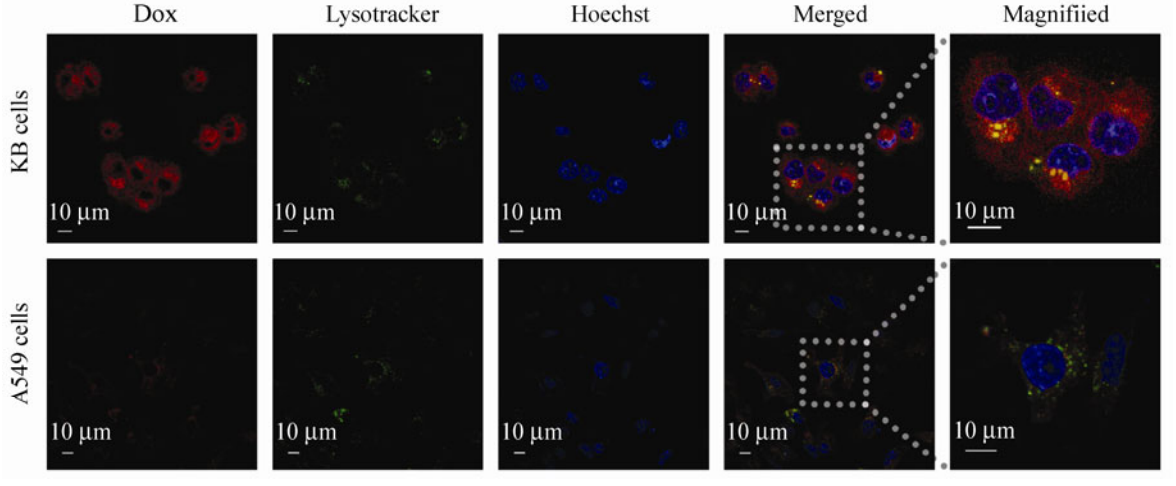

Figure 6 Confocal laser scanning microscopy images of HMP–FA–DOX in KB cells and A549 cells. Blue parts are nuclei, stained with Hoechst 33342, and green parts are lysosomes, stained with LysoTracker Green DND-26. Magnified figures are the enlargements of cells within rectangles in merged figures

survival was observed. In contrast, the differences between HMP–FA–DOX, HMP–DOX and FA-pretreated HMP–FA–DOX with HeLa cells were smaller (Fig. 7(c)), and negligible with A549 cells (Fig. 7(d)). Additionally, for the same drug concentration and exposure time, the viability of HMP–FA–DOX treated cells decreased in the order A549 cells > HeLa cells > KB cells, which reveals the enhanced cytotoxicity stems from the high cellular uptake of HMP–FA–DOX in a FR-mediated endocytosis mechanism and efficient drug release upon engulfing, as discussed before. It should be mentioned that the viability of free DOX-treated cells were low in all three cell lines, however, in HMP–FA–DOX NPs, the viability in normal cells (FR-negative cells) remained high. These characteristics of targeted DOX delivery and selective inhibition of cell proliferation are crucial in a drug delivery system, and makes HMP–FA–DOX an ideal carrier for effective drug delivery.

3.5 *In vitro* MR imaging

Finally, to evaluate the feasibility of using MRI to track the delivery of HMP NPs, MRI signal intensities of HMP–FA–DOX treated KB cells, HeLa cells, and A549 cells were examined using a 1.5 T MRI system. As shown in Fig. 8(a), the T_1-weighted MRI of KB cells treated with NPs showed the brightest signal, followed by HeLa cells, and little appreciable signal enhancement was observed with A549 cells. In contrast, the brightness dropped severely when FR

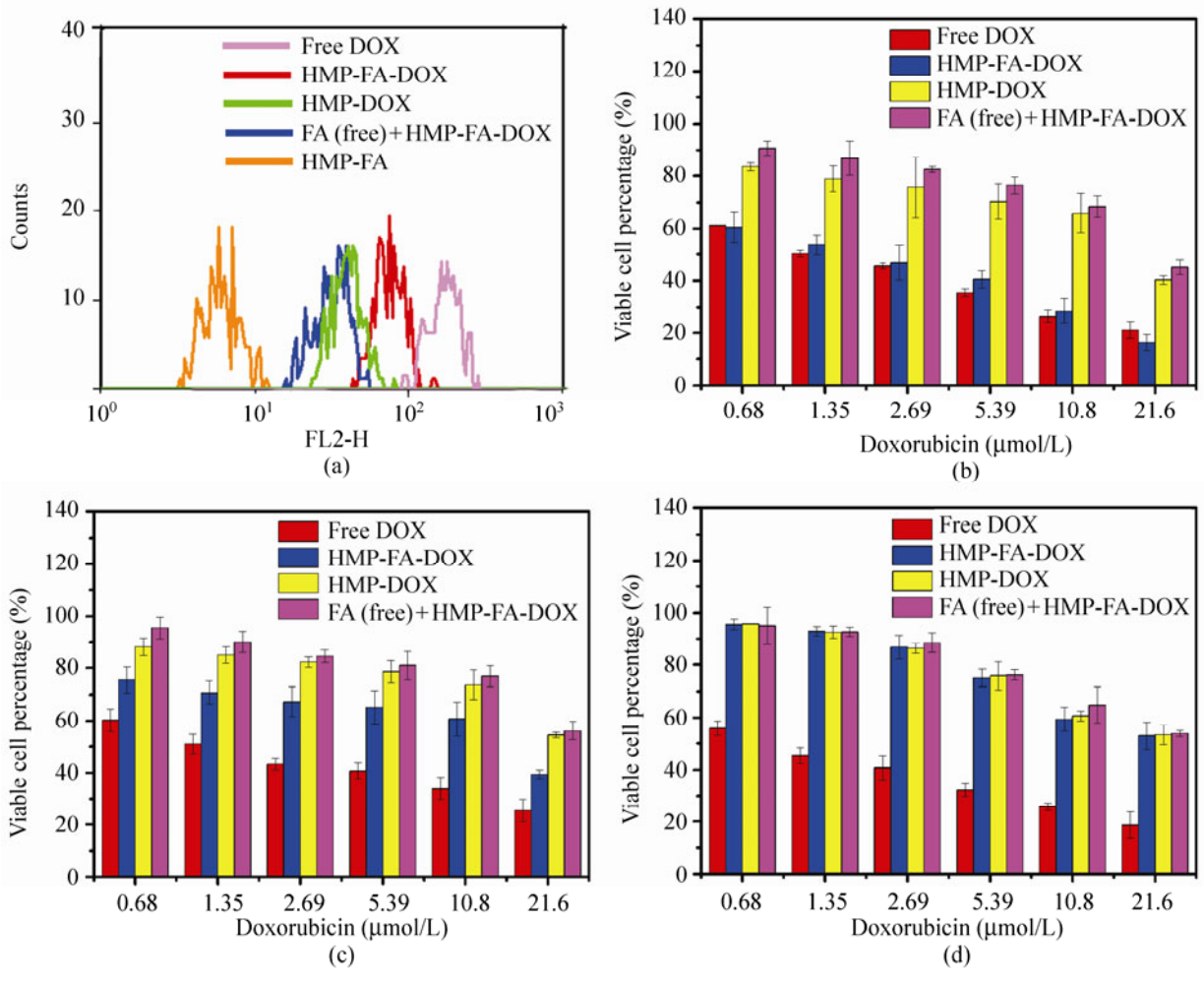

Figure 7 (a) Flow cytometry profiles of fluorescence from DOX in KB cells. Cells were incubated with free DOX, HMP–FA–DOX, HMP–DOX, and FA-saturated HMP–FA–DOX NPs. Background of KB cells were attained by treating cells with HMP–FA without DOX. MTT assay of free DOX, HMP–FA–DOX, HMP–DOX, and FA-saturated HMP–FA–DOX with (b) KB cells, (c) HeLa cells, and (d) A549 cells containing the same amount of DOX. Error bars are based on standard deviations of six parallel samples

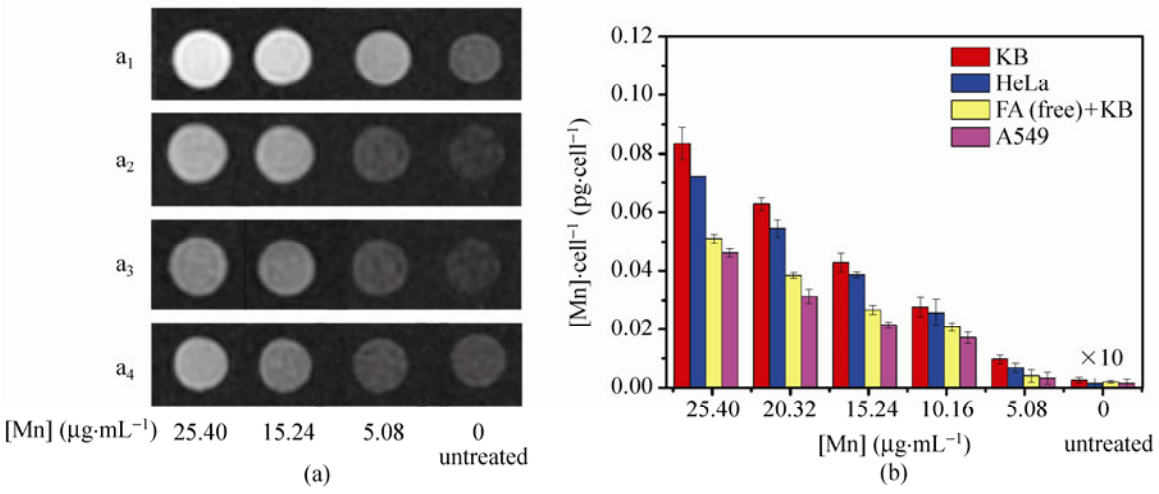

Figure 8 (a) T_1-weighted MRI of HMP–FA–DOX after incubation with (a_1) KB cells, (a_2) HeLa cells, (a_3) A549 cells, and (a_4) FA pre-saturated KB cells. (b) Cellular uptake of HMP–FA–DOX examined by ICP–AES against manganese concentration. Error bars are based on standard deviations of triplicated samples. The manganese concentrations in untreated cells are magnified ten times

pre-saturated KB cells were internalized with NPs. This result implies that the targeted manganese cellular uptake could be examined by MR imaging. To verify this result, ICP–AES was also employed (Fig. 8(b)). As expected, the cellular uptake of manganese decreased in of the order KB cells > HeLa cells > FA pre-treated KB cells > A549 cells, in agreement with what was observed by MRI. These results suggest that HMP–FA–DOX can not only give effectively targeted delivery of DOX, but can also be used to track the delivery effect through T_1-weighted MRI. Consequently, HMP–FA–DOX can act as a multifunctional probe for cancer cell targeted MRI and pH-triggered drug delivery.

4. Conclusion

We have successfully synthesized neoteric FA-targeted hollow manganese phosphate nanoparticles loaded with the anti-tumor drug DOX, which showed pH-triggered drug delivery and pH-convertible MRI contrast effects. Our results suggest that DOX is mostly loaded into the hollow part, and released through a pH-controlled pathway, i.e. more drug is released at low pH. A remarkable improvement in MR relaxivity (both in r_1 and r_2) at low pH (pH 5.4) compared to that in a neutral environment (pH 7.4) was achieved, because HMP NPs dissolved giving Mn^{2+} at low pH. After conjugation of FA with HMP NPs, the FA–HMP NPs could be recognized by the FA-positive cells through FR-mediated endocytosis. The MTT assay suggested that HMP–FA–DOX could inhibit KB cells more severely than HeLa cells and A549 cells, making it possible minimize the side effects on normal cells. The delivery process could also be tracked by MRI, which highlights the potential of this material to form a multifunctional probe for MRI and pH-triggered drug delivery.

Acknowledgements

This work was supported in part by National Natural Science Foundation of China (NSFC) (Nos. 51125001, 51172005, 90922033, and 21105120), the National Basic Research Program of China (No. 2010CB934601), the Doctoral Program (No. 20090001120010) and New Century Talent of the Education Ministry of China (No. NCET-09-0177), the Fok Ying Tung Education Foundation (No. 122043), and the New Star Program of Beijing Municipal Science and Technology Commission (BCST) (No. 2008B02).

Electronic Supplementary Material: XRD patterns and TEM image of HMP NPs, FTIR, and thermogravimetric/differential thermagravimetric (TG/DTG) image of APS–PEG–COOH and APS–PEG–FA, TEM image and hydrodynamic size distribution of HMP NPs

dispersed in pH 5.4 and pH 7.4 buffer, ICP–AES of manganese content in supernatant and sedimentation of HMP after centrifugation with 15 000 r/min at pH 5.4 and pH 7.4, r_2 relaxivity and MRI for $MnCl_2$, and manganese concentration in supernatant of HMP at pH 5.4 before and after annealing at 500 ℃ are available in the online version of this article at http://dx.doi.org/10.1007/s12274-012-0252-z

References

[1] Louie, A. Multimodality imaging probes: Design and challenges. *Chem. Rev.* **2010**, *110*, 3146–3195.

[2] Jarzyna, P. A.; Gianella, A.; Skajaa, T.; Knudsen, G.; Deddens, L. H.; Cormode, D. P.; Fayad, Z. A.; Mulder, W. J. M. Multifunctional imaging nanoprobes. *Wiley Interdiscip. Rev.: Nanomed. Nanobiotechnol.* **2010**, *2*, 138–150.

[3] Dubertret, B.; Skourides, P.; Norris, D. J.; Noireaux, V.; Brivanlou, A. H.; Libchaber, A. *In vivo* imaging of quantum dots encapsulated in phospholipid micelles. *Science* **2002**, *298*, 1759–1762.

[4] Nam, J. M.; Thaxton, C. S.; Mirkin, C. A. Nanoparticle-based bio-bar codes for the ultrasensitive detection of proteins. *Science* **2003**, *301*, 1884–1886.

[5] Jin, Y.; Jia, C.; Huang, S. W.; O'Donnell, M.; Gao, X. Multifunctional nanoparticles as coupled contrast agents. *Nat. Commun.* **2010**, *1*, 41.

[6] Veiseh, O.; Gunn, J. W.; Zhang, M. Design and fabrication of magnetic nanoparticles for targeted drug delivery and imaging. *Adv. Drug Delivery Rev.* **2010**, *62*, 284–304.

[7] Wang, F.; Han, Y.; Lim, C. S.; Lu, Y. H.; Wang, J.; Xu, J.; Chen, H. Y.; Zhang, C.; Hong, M. H.; Liu, X. G. Simultaneous phase and size control of upconversion nanocrystals through lanthanide doping. *Nature* **2010**, *463*, 1061–1065.

[8] Hao, R.; Xing, R.; Xu, Z.; Hou, Y.; Gao, S.; Sun, S. Synthesis, functionalization, and biomedical applications of multifunctional magnetic nanoparticles. *Adv. Mater.* **2010**, *22*, 2729–2742.

[9] Xie, J.; Liu, G.; Eden, H. S.; Ai, H.; Chen, X. Surface-engineered magnetic nanoparticle platforms for cancer imaging and therapy. *Acc. Chem. Res.* **2011**, *44*, 883–892.

[10] Ho, D.; Sun, X.; Sun, S. Monodisperse Magnetic nanoparticles for theranostic applications. *Acc. Chem. Res.* **2011**, *44*, 875–882.

[11] Na, H. B.; Lee, J. H.; An, K. J.; Park, Y. I.; Park, M.; Lee, I. S.; Nam, D. H.; Kim, S. T.; Kim, S. H.; Kim, S. W.; Lim, K. H.; Kim, K. S.; Kim, S. O.; Hyeon, T. Development of a T_1 contrast agent for magnetic resonance imaging using MnO nanoparticles. *Angew. Chem. Int. Ed.* **2007**, *46*, 5397–5401.

[12] Hu, F.; Jia, Q.; Li, Y.; Gao, M. Facile synthesis of ultrasmall PEGylated iron oxide nanoparticles for dual-contrast T_1- and T_2-weighted magnetic resonance imaging. *Nanotechnology* **2011**, *22*, 245604.

[13] Kim, T.; Momin, E.; Choi, J.; Yuan, K.; Zaidi, H.; Kim, J.; Park, M.; Lee, N.; McMahon, M. T.; Quinones-Hinojosa, A. et al. Mesoporous silica-coated hollow manganese oxide nanoparticles as positive T_1 contrast agents for labeling and MRI tracking of adipose-derived mesenchyrnal stem cells. *J. Am. Chem. Soc.* **2011**, *133*, 2955–2961.

[14] Xing, R.; Liu, G.; Quan, Q.; Bhirde, A.; Zhang, G.; Jin, A.; Bryant, L. H.; Zhang, A.; Liang, A.; Eden, H. S. et al. Functional MnO nanoclusters for efficient siRNA delivery. *Chem. Commun.* **2011**, *47*, 12152–12154.

[15] Huang, C. C.; Khu, N. H.; Yeh, C. S. The characteristics of sub 10 nm manganese oxide T(1) contrast agents of different nanostructured morphologies. *Biomaterials* **2010**, *31*, 4073–4078.

[16] Xing, R.; Zhang, F.; Xie, J.; Aronova, M.; Zhang, G.; Guo, N.; Huang, X.; Sun, X.; Liu, G.; Bryant, L. H.; Bhirde, A. el al. Polyaspartic acid coated manganese oxide nanoparticles for efficient liver MRI. *Nanoscale* **2011**, *3*, 4943–4935.

[17] Caravan, P. Strategies for increasing the sensitivity of gadolinium based MRI contrast agents. *Chem. Soc. Rev.* **2006**, *35*, 512–523.

[18] Ha, T. L.; Kim, H. J.; Shin, J.; Im, G. H.; Lee, J. W.; Heo, H.; Yang, J.; Kang, C. M.; Choe, Y. S.; Lee, J. H. et al. Development of target-specific multimodality imaging agent by using hollow manganese oxide nanoparticles as a platform. *Chem. Commun.* **2011**, *47*, 9176–9178.

[19] Shin, J. M.; Md Anisur, R.; Ko, M. K.; Im, G. H.; Lee, J. H.; Lee, I. S. Hollow manganese oxide nanoparticles as multifunctional agents for magnetic resonance imaging and drug delivery. *Angew. Chem. Int. Ed.* **2009**, *48*, 321–324.

[20] Chen, Y.; Chu, C.; Zhou, Y.; Ru, Y.; Chen, H.; Chen, F.; He, Q.; Zhang, Y.; Zhang, L.; Shi, J. Reversible pore-structure evolution in hollow silica nanocapsules: Large pores for siRNA delivery and nanoparticle collecting. *Small* **2011**, *7*, 2935–2944.

[21] Chen, Y.; Chen, H.; Zhang, S.; Chen, F.; Zhang, L.; Zhang, J.; Zhu, M.; Wu, H.; Guo, L.; Feng, J.; Shi, J. Multifunctional mesoporous nanoellipsoids for biological bimodal imaging and magnetically targeted delivery of anticancer drugs. *Adv. Funct. Mater.* **2011**, *21*, 270–278.

[22] Wu, H.; Zhang, S.; Zhang, J.; Liu, G.; Shi, J.; Zhang, L.; Cui, X.; Ruan, M.; He, Q.; Bu, W. A hollow-core, magnetic, and mesoporous double-shell nanostructure: *In situ* decomposition/reduction synthesis, bioimaging, and drug-delivery properties. *Adv. Funct. Mater.* **2011**, *21*, 1850–1862.

[23] Du, J. Z.; Du, X. J.; Mao, C. Q.; Wang, J. Tailor-made dual

pH-sensitive polymer–doxorubicin nanoparticles for efficient anticancer drug delivery. *J. Am. Chem. Soc.* **2011**, *133*, 17560–17563.

[24] Lee, E. S.; Oh, K. T.; Kim, D.; Youn, Y. S.; Bae, Y. H. Tumor pH-responsive flower-like micelles of poly(l-lactic acid)-b-poly(ethylene glycol)-b-poly(l-histidine). *J. Control. Release* **2007**, *123*, 19–26.

[25] Wu, W.; Shen, J.; Banerjee, P.; Zhou, S. Chitosan-based responsive hybrid nanogels for integration of optical pH-sensing, tumor cell imaging and controlled drug delivery. *Biomaterials* **2010**, *31*, 8371–8381.

[26] Tang, H.; Guo, J.; Sun, Y.; Chang, B.; Ren, Q.; Yang, W. Facile synthesis of pH sensitive polymer-coated mesoporous silica nanoparticles and their application in drug delivery. *Int. J. Pharm.* **2011**, *421*, 388–396.

[27] He, Q.; Gao, Y.; Zhang, L.; Bu, W.; Chen, H.; Li, Y.; Shi, J. One-pot self-assembly of mesoporous silica nanoparticle-based pH-responsive anti-cancer nano drug delivery system. *J. Mater. Chem.* **2011**, *21*, 15190–15192.

[28] Shapiro, E. M.; Koretsky, A. P. Convertible manganese contrast for molecular and cellular MRI. *Magn. Reson. Med.* **2008**, *60*, 265–269.

[29] Bennewitz, M. F.; Lobo, T. L.; Nkansah, M. K.; Ulas, G.; Brudvig, G. W.; Shapiro, E. M. Biocompatible and pH-Sensitive PLGA Encapsulated MnO Nanocrystals for Molecular and Cellular MRI. *ACS Nano* **2011**, *5*, 3438–3446.

[30] Sudimack, J.; Lee, R. J. Targeted drug delivery via the folate receptor. *Adv. Drug Delivery Rev.* **2000**, *41*, 147–162.

[31] Zhang, Y.; Kohler, N.; Zhang, M. Surface modification of superparamagnetic magnetite nanoparticles and their intracellular uptake. *Biomaterials* **2002**, *23*, 1553–1561.

[32] Hao, R.; Yu, J.; Hou, Y.; Sun, S. One-pot synthesis of hollow/porous Mn-based nanoparticles via a controlled ion transfer process. *Chem. Commun.* **2011**, *47*, 9095–9097.

[33] De Palma, R.; Peeters, S.; Van Bael, M. J.; Van den Rul, H.; Bonroy, K.; Laureyn, W.; Mullens, J.; Borghs, G.; Maes, G. Silane ligand exchange to make hydrophobic superparamagnetic nanoparticles water-dispersible. *Chem. Mater.* **2007**, *19*, 1821–1831.

[34] Liu, Z.; Fan, A. C.; Rakhra, K.; Sherlock, S.; Goodwin, A.; Chen, X.; Yang, Q.; Felsher, D. W.; Dai, H. Supramolecular stacking of doxorubicin on carbon nanotubes for *in vivo* cancer therapy. *Angew. Chem. Int. Ed.* **2009**, *48*, 7668–7672.

[35] Wang, C.; Cheng, L.; Liu, Z. Drug delivery with upconversion nanoparticles for multi-functional targeted cancer cell imaging and therapy. *Biomaterials* **2011**, *32*, 1110–1120.

[36] Cheng, Z.; Chen, A. K.; Lee, H. Y.; Tsourkas, A. Examination of folate-targeted liposomes with encapsulated poly(2-propylacrylic acid) as a pH-responsive nanoplatform for cytosolic drug delivery. *Small* **2010**, *6*, 1398–1401.

[37] Mao, J.; Gan, Z. The influence of pendant hydroxyl groups on enzymatic degradation and drug delivery of amphiphilic poly[glycidol-block-(ε-caprolactone)] copolymers. *Macromol. Biosci.* **2009**, *9*, 1080–1089.

[38] Coluccio, M. L.; Ciardelli, G.; Bertoni, F.; Silvestri, D.; Cristallini, C.; Giusti, P.; Barbani, N. Enzymatic erosion of bioartificial membranes to control drug delivery. *Macromol. Biosci.* **2006**, *6*, 403–411.

[39] Luo, Z.; Cai, K.; Hu, Y.; Li, J.; Ding, X.; Zhang, B.; Xu, D.; Yang, W.; Liu, P. Redox-responsive molecular nanoreservoirs for controlled intracellular anticancer drug delivery based on magnetic nanoparticles. *Adv. Mater.* **2012**, *24*, 431–435.

[40] Luo, Z.; Cai, K.; Hu, Y.; Zhao, L.; Liu, P.; Duan, L.; Yang, W. Mesoporous silica nanoparticles end-capped with collagen: Redox-responsive nanoreservoirs for targeted drug delivery. *Angew. Chem. Int. Ed.* **2011**, *50*, 640–643.

[41] Tang, S.; Huang, X.; Chen, X.; Zheng, N. Hollow mesoporous zirconia nanocapsules for drug delivery. *Adv. Funct. Mater.* **2010**, *20*, 2442–2447.

[42] Canal, F.; Vicent, M. J.; Pasut, G.; Schiavon, O. Relevance of folic acid/polymer ratio in targeted PEG–epirubicin conjugates. *J. Control. Release* **2010**, *146*, 388–399.

[43] Gravier, J.; Schneider, R.; Frochot, C.; Bastogne, T.; Schmitt, F.; Didelon, J.; Guillemin, F.; Barberi-Heyob, M. Improvement of meta-tetra(Hydroxyphenyl)chlorin-like photosensitizer selectivity with folate-based targeted delivery. Synthesis and *in vivo* delivery studies. *J. Med. Chem.* **2008**, *51*, 3867–3877.

[44] Koretsky, A. P.; Silva, A. C. Manganese-enhanced magnetic resonance imaging (MEMRI). *NMR Biomed.* **2004**, *17*, 527–531.

[45] Mukhopadhyay, S.; Linstedt, A. D. Identification of a gain-of-function mutation in a Golgi P-type ATPase that enhances Mn(2+) efflux and protects against toxicity. *Proc. Natl. Acad. Sci. U. S. A.* **2011**, *108*, 858–863.

[46] Pan, D.; Schmieder, A. H.; Wickline, S. A.; Lanza, G. M. Manganese-based MRI contrast agents: Past, present, and future. *Tetrahedron* **2011**, *67*, 8431–8444.

[47] Liu, Y.; Mi, Y.; Zhao, J.; Feng, S. S. Multifunctional silica nanoparticles for targeted delivery of hydrophobic imaging and therapeutic agents. *Int. J. Pharm.* **2011**, *421*, 370–378.

[48] Tong, R.; Cheng, J. Anticancer polymeric nanomedicines. *Polym. Rev.* **2007**, *47*, 345–381.

[49] Yoo, H. S.; Park, T. G. Folate-receptor-targeted delivery of doxorubicin nano-aggregates stabilized by doxorubicin–PEG–folate conjugate. *J. Control. Release* **2004**, *100*, 247–256.

[50] Guo, M.; Que, C.; Wang, C.; Liu, X.; Yan, H.; Liu, K. Multifunctional superparamagnetic nanocarriers with folate-mediated and pH-responsive targeting properties for anticancer drug delivery. *Biomaterials* **2011**, *32*, 185–194.